SSC24-P1-09

Development of a Methodology for Optimizing Satellite Durability by Coupling Advanced Orbit Propagation with High Fidelity 3D Thermal-Electrical Simulation

Corey D. Packard[1], Logan R. Canull[1], Zachary J. Edel[1], Timofey Golubev[1], Michael L. Larsen[1,2,3]
[1] ThermoAnalytics, Inc., 23440 Airpark Blvd, Calumet, MI 49913
cdp@thermoanalytics.com

[2] Department of Physics and Astronomy, College of Charleston, 66 George St., Charleston, SC 29424

[3] Department of Physics and Atmospheric Sciences Program, Michigan Technological University
1400 Townsend Dr., Houghton, MI 49931

Nate McCoun
a.i. solutions, 4500 Forbes Blvd, Suite 300, Lanham, MD 20706
nate.mccoun@ai-solutions.com

ABSTRACT

In the rapidly evolving landscape of low Earth orbit (LEO) satellite technology, this study presents a pioneering approach for analyzing satellite durability through advanced orbit propagation and high fidelity 3D thermal-electric simulation. Small satellites, packed with high power components and rapidly transitioning between sunlit and eclipsed orbit segments, often feature limited thermal control systems that make thermal management a challenging (but critical) task. Additionally, the durability of battery cells and photovoltaic (PV) panels over the mission lifetime of small satellites is an important concern. Cycling and calendar fade take their toll on battery lifetime, and PV degradation reduces operational efficiency over time as well. Our research aims to develop a modeling approach for optimizing satellite resilience and operational efficiency by addressing critical factors such as battery lifetime, PV degradation and position/attitude correction automation.

Our approach to dynamic satellite simulation predicts in-orbit transient temperatures while considering PV-captured solar power, electronic loads and battery charging/discharging. A high fidelity simulation process obtains coupled thermal-electrical solutions by combining a 3D surface/volume mesh with appropriate thermal material properties and active heat sources. A battery management system is included to control battery cell discharging (due to electrical loads) and charging based on battery charge status and the availability of harvested solar energy from PV panels. PV module temperatures (as well as solar incidence angle and degradation) are used to calculate solar power conversion efficiency, which influences the available supplied power for electronics and battery charging. Declines in battery performance, characterized by reduced battery capacity and increased internal resistance, are considered based on battery lifetime predictions. Process automation software manages the simulation of satellites by incorporating propagation tools that provide orbital boundary conditions to the transient thermal-electrical solver. In addition, the orbital propagation tool can provide adaptations to the fluctuating and harsh LEO environment, including dynamic satellite positioning and minimizing exposure to radiation and other environmental stressors.

The result of this coupled approach is a comprehensive study of satellite durability against the thermal challenges inherent to LEO. This methodology considers both the inter-dependent relationship between electrical performance and thermal environments and the inevitable degradation of PV efficiency and battery performance over time, informing deliberate decisions regarding material selection and thermal control strategies. This helps ensure temperatures of critical components (including battery cells) remain inside operational limits and extend satellite mission lifetimes by avoiding unnecessary stresses that impact durability. Our research findings showcase a significant advancement in the ability to predict and improve satellite durability by mitigating the impact of environmental stress on critical components. By combining sophisticated orbit propagation with advanced energy generation and storage simulation capabilities, our approach contributes to the sustainability of satellite missions in LEO, reducing operational costs and environmental impact. This study not only presents innovative predictive capabilities but also underscores the importance of developing resilient satellite systems for the future of orbital infrastructure.

INTRODUCTION

As the landscape of low Earth orbit (LEO) changes with the ever-increasing launch of small satellites, the need has intensified for predicting the thermal-electrical performance of satellites. Small satellites often contain a high density of components with significant power demands, making thermal management (either passive or active) a key concern. The thermal environment surrounding a battery impacts its electrical performance, and the electrical conditions of a battery also influence its pack temperature. The efficiency of a photovoltaic module changes as its temperatures oscillate and the incidence angle of solar radiation changes during an orbit. Similarly, photovoltaic temperatures are impacted by the efficiency with which they are able to convert absorbed solar energy to electrical power. Thus, a predictive approach that incorporates both thermal and electrical calculations during dynamic orbits in a coupled, multi-physics method is required.

Additionally, the ability to not only predict ideal satellite performance (i.e., expected performance when all components are in new condition) but also end-of-life performance (i.e., later in the satellite mission lifetime when the battery and photovoltaic modules have degraded) is highly desirable. Consequently, the durability of both photovoltaic (PV) modules and battery cells over the mission lifetime of the satellite must be incorporated into predictive simulation workflows. Calendar fade (deterioration due to battery age) and cycling fade (deterioration due to battery usage) are primary battery lifetime concerns, as elevated internal resistance and reduced pack capacity combine to negatively affect battery performance over time. Radiation-induced degradation of PV efficiency (due to extended exposure to subatomic particles during orbit and over time) must also be examined and included.

This work presents a dynamic satellite simulation approach that predicts in-orbit temperatures while incorporating PV-converted solar power, electronic component loads necessary to fulfill the satellite mission, and battery charging/discharging during sunlit/eclipsed orbital segments. This automated high-fidelity process combines 3D geometry, material properties and active heat source data with a transient thermal-electrical coupled solver, employing orbit propagator-supplied boundary conditions. A battery management system is included to control battery cell charging/discharging, and a PV controller limits solar-supplier energy based on efficiency, battery status and component power needs. We develop a methodology for addressing mission durability concerns such as battery lifetime and PV efficiency degradation, providing an avenue for future optimization of satellite resilience and operational efficiency. These optimizations could include orbital adaptations to mitigate the fluctuating and harsh LEO environment, including dynamic satellite positioning and radiation exposure minimization.

We describe the thermal-electrical results obtained by simulating a LEO satellite, in motion, both at the beginning of its mission as well as near the end of its useful orbital lifetime. We show the impact of the inevitable decline in battery performance and PV-module efficiency and highlight ways in which the satellite lifetime could potentially be extended, including thermal control strategies and orbital adjustments. Our methodology and findings showcase an advancement in satellite performance predictions, mission lifetime estimations and evaluation of mission extension concepts.

In the Methodology section we provide an overview of our high-fidelity approach, introduce the tools and describe the simulation model and boundary conditions used for the analysis performed during this effort. In the Analysis and Results section we present the results of the initial (baseline) and degraded (end-of-life) simulations, with a description of the battery lifetime and PV degradation process employed. Finally, in the Summary section we discuss our research findings and note some future work suggested by our conclusions thus far.

METHODOLOGY

Overview of Thermal-Electrical Coupled Simulation

The dynamic prediction of orbiting satellites is performed by MuSES™, a transient thermal-electrical and EO/IR simulation software designed for a wide variety of high-fidelity commercial applications. Coupled thermal-electrical satellite simulations are managed by CoTherm™, a process automation software package able to flexibly exchange data with a wide variety of 3rd party applications. The dynamic orbital boundary conditions necessary for thermal and electrical predictions are supplied to CoTherm via the orbit propagation tool FreeFlyer®. CoTherm computes the environmental boundary conditions (e.g., solar loading and position of the sun and Earth relative to the satellite) for MuSES based on FreeFlyer's orbit propagation. MuSES executes the dynamic simulation of the orbiting satellite based on this orbital data, and CoTherm post-processes the results and documents the relevant simulation inputs and resultant outputs. Figure 1 illustrates the CoTherm simulation automation process used to manage the satellite thermal-electrical analysis presented in this work.

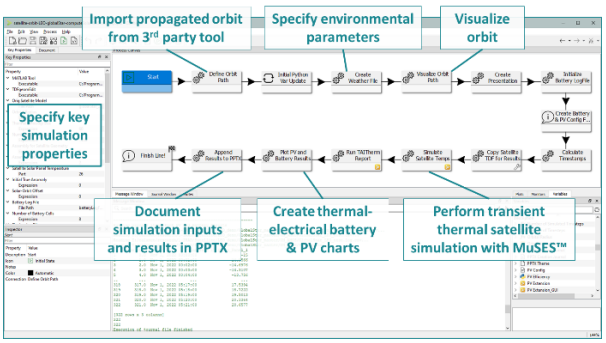

Figure 1: CoTherm-based Satellite Process

In the remainder of this section we detail the transient simulation software used to predict satellite temperatures and electrical performance, the orbit propagation software used to define the path and attitude of the satellite, and the 3D simulation model used for the study presented in this work.

Transient Simulation Software: MuSES

MuSES™ (**Mu**lti-**S**ervice **E**lectro-Optic **S**ignature) is a commercial thermal and infrared simulation software application[1-3] developed by ThermoAnalytics that uses first principles physics to predict heat transfer due to radiation, conduction, and convection. A surface or volume mesh describes the system geometry and is used for radiation exchange calculations via automatic view factor generation. Lateral and vertical conduction is handled via automatic nodal network generation from this same mesh, though alternative thermal links can also be defined to specify additional conduction paths.

Thermal material properties including thermal conductivity, density and specific heat are applied to each component to characterize the transient thermal response to supplied (orbital) boundary conditions. Optical surface properties including solar absorptivity, thermal emissivity (and spectral diffuse/specular reflectivity if desired) are specified for each surface to govern radiation exchange. Heat sources such as circuit boards, amplifiers, batteries, antennae and other internal/external components can be defined as constant values, time-dependent curves or controlled with Python-based user routines. Convection can be included in a variety of ways depending on the desired fidelity; methods include the use of bulk fluid nodes or fluid streams with textbook fluid flow correlations, mapping imported computational fluid dynamics (CFD) results onto surfaces, and the use of the native RapidFlow™ 3D flow solver.

Physical temperatures are calculated for each node in the model at each discrete timestep in the transient simulation. These dynamic temperatures are impacted by the movement of the sun relative to the satellite, radiation from the Earth, radiation losses to space, component heating, thermal capacitance and passive/active thermal control strategies. MuSES-predicted temperature results for a 3U CubeSat in LEO have been compared against published literature favorably, with temperature discrepancies falling within the same range (within 0.2°C for that orbit) as other simulation tools used by space agencies.[4]

Battery and PV Methodology in MuSES

MuSES is also capable of integrating batteries and PV panels into thermal simulations via a coupled thermal-electrical multi-physics solution. Battery cells and solar panels can be represented several ways in MuSES, depending on the available component information and fidelity required. For example, an equivalent circuit approach for both batteries and PV panels is possible. This method is diagramed in Figure 2, with a PV equivalent circuit shown (left) alongside a battery equivalent circuit (right).

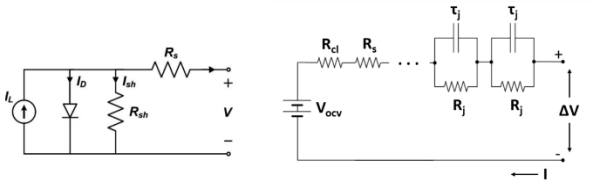

Figure 2: PV and battery equivalent circuits

MuSES solves both the thermal and electrical problems concurrently, due to the multi-physics nature of such a simulation. This methodology results in accurate prediction of PV efficiency and harvested solar energy, battery current/power/SoC (state of charge) information, and temperature predictions for both of these vital systems as well as other electronic components.

Battery cell heating is dependent on temperature and vice versa.[5-7] The current through each battery cell is dependent on the electrical boundary conditions (e.g., voltage, current or power) and the state of the cell which includes cell temperature and depth of discharge (which is the complement of state of charge). The heat generated in a battery cell is calculated based on both irreversible (Joule heating) and reversible (entropic heating) terms. These heat rates are dependent on the current through the battery cell as well as the temperature-dependent state of that battery cell, and are used by the MuSES thermal solver to calculate the evolution of battery cell temperatures during transient simulations.

Similarly, PV-generated power is also temperature dependent, so a coupled thermal-electrical PV model[8] analogous to that described for battery packs is employed by MuSES. For this work, instead of using an equivalent circuit approach, the PV electrical behavior was modeled

using the nominal efficiency and temperature coefficient approach described in Ref. 8. PV electrical calculations are performed for each thermal simulation timestep, using the updated module temperatures and solar incidence angles. The dynamic efficiency of PV modules is used to calculate the maximum amount of photogenerated energy available for powering active components and battery charging, but the actual value of harvested solar energy is limited by the component load when the battery is fully charged. Thus, during sunlit portions of the orbit, the PV panels convert solar energy to electrical power which is used to operate electrical components (as dictated by the mission) and charge battery cells (when necessary). During eclipsed regions when the satellite is in the Earth's shadow, the PV energy production falls to zero and the battery alone must be capable of powering any active components.

Battery performance degrades over time due to a variety of causes.[9] The stress factors involved include charging and discharging history (i.e., battery usage and maintenance), thermal environmental stresses during the life of the battery, and calendar fade (which happens over time, regardless of usage).[10] In general these causal factors lead to increased battery internal resistance and reduced battery capacity, degrading the performance of the battery over time compared to its "showroom" condition.[11]

In addition, the performance of PV modules deployed in low-earth orbit degrades due to exposure to space radiation, namely high-energy electrons and protons. These high energy particles can cause significant damage to PV modules mainly through atomic displacement and ionization damage.[12] Atomic displacement refers to the displacement of atoms within the crystal lattice of solar cells, creating defects that degrade its electrical and optical properties. Ionization damage refers the removal of electrons from their orbitals, which can cause multiple detrimental effects such as charge accumulations that alter the electric field that drives the separation and collection of photogenerated charge carriers, reducing efficiency.

Our approach includes the ability to predict battery lifetime by estimating how battery internal resistance and capacity may change with time, usage and temperature extremes.[13] These changes are then incorporated into subsequent simulations of battery performance based on these lifetime predictions. Additionally, we estimate radiation exposure of PV modules in orbit and, as a result, predict the degraded PV efficiency to simulate the impact of reduced photovoltaic performance.

As a final note on the transient thermal simulation software used for the analysis presented in this work, it is important to clarify that beyond predicting temperatures, MuSES can calculate EO/IR signatures across the 0.4 – 20 micron spectrum (i.e., visible through long-wave infrared). This infrared signature prediction capability is what makes MuSES export-controlled; another version of this software package, referred to as TAITherm, is well-known in the automotive and transportation industries but is not able to make electro-optic/infrared sensor radiance predictions. This work uses the MuSES moniker with which the space and defense audience is more familiar.[14]

Communications Satellite Model

For the study presented in this work, a simulation model of a communications satellite was produced. Three-dimensional CAD (computer-aided design) geometry was created for the satellite body, external components and PV panels. Subsquently, a surface mesh was generated to ensure that a proper radiation and conduction nodal network would be automatically generated. Each part (a set of elements sharing material properties and boundary conditions) is shown with a different color, and mesh edges are hidden for visual clarity. Overall, the communication satellite model (shown in Figure 3) has dimensions of 6.5m x 2.7m x 1.1m and comprises 34 parts and 262,184 surface elements.

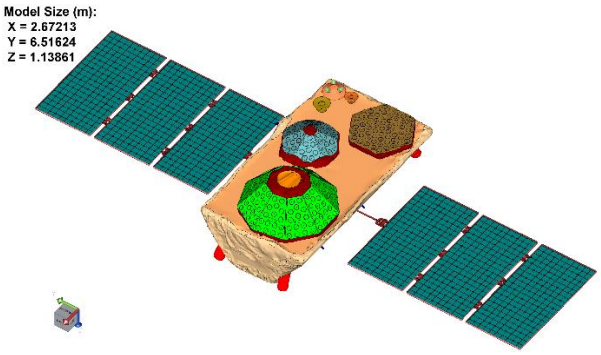

Figure 3: Communications Satellite Model

A variety of external components are labeled in Figure 4, including the PV panels and communication antennae. The PV panels represent triple-junction solar cells covering a total surface area of 5.64 m^2 with a nominal efficiency of 29% that varies over the course of an orbit and throughout the spacecraft mission lifetime.

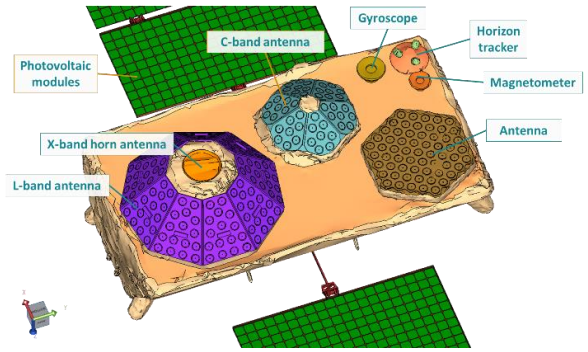

Figure 4: Satellite External Components

Many of the critical internal components are shown in Figure 5 including the battery pack, amplifiers and transponders, flight computer, etc.

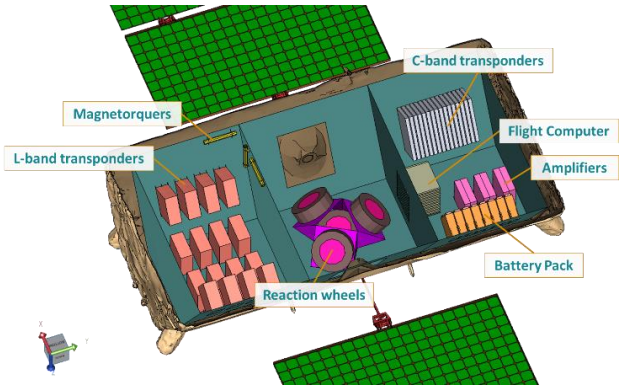

Figure 5: Satellite Internal Components

Each powered component was assigned an individual efficiency and mission-based time-dependent heat rate. The combination of these component-specific transient functions was used to compute the total system power draw on the PV modules and battery, shown in Figure 6.

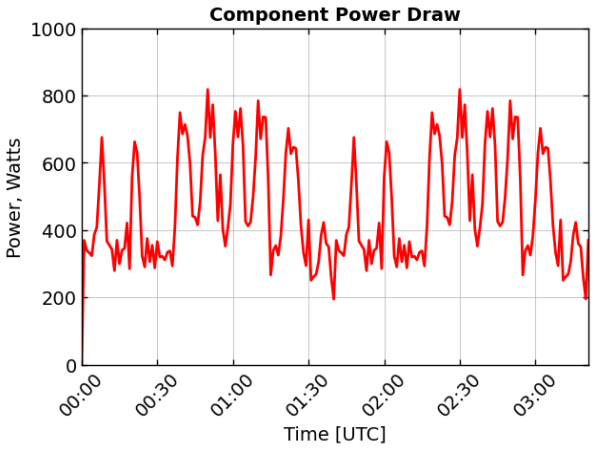

Figure 6: Total Component Power Load

This total system power draw is periodic in nature, with an average power of 467.4 W during a period of approximately 95 minutes. Only the first two periods are shown in Figure 6 to increase the legibility of the line plot. To provide power during eclipsed regions of the orbit, the spacecraft system employs a 54 A-hr Li-ion battery pack.

Orbit Propagation: FreeFlyer

The dynamic orbital boundary conditions necessary for thermal and electrical predictions are supplied to CoTherm™ via the orbit propagation tool FreeFlyer®. FreeFlyer is a tool for spacecraft mission design and analysis. As spacecraft are dynamic objects, a mission design and analysis tool must simulate their motion, both spatially and temporally. FreeFlyer uses a "Propagator" object to model spacecraft motion.

Given an initial state (see Table 1), FreeFlyer produced a high-fidelity custom ephemeris with celestial body positions that could be read into CoTherm. Considering both nominal and decaying conditions were tested in CoTherm's simulations, a combination of Runge Kutta 8(9) and Bulirsch Stoer integrators were selected for product generation in FreeFlyer.

Table 1: Initial State Conditions

Parameter	Value
Epoch	Jun 01 2024 00:00:00.000
Reference Frame	TEME (True Equator Mean Equinox)
X	2190.80891 km
Y	4249.62858 km
Z	4714.08058 km
VX	-1.30199 km/s
VY	-5.33264 km/s
VZ	5.41232 km/s

The integration algorithms are used in conjunction with a high-fidelity force model that includes parameters related to gravitational and atmospheric forces.

Due to the Earth's non-spherical shape and non-uniform density profile, its gravitational field can be derived from a potential function (the geopotential) that depends on the radial distance and the angular location of the spacecraft with respect to the center of mass of the Earth. The Earth's equatorial bulge and the flattening of the poles produce the dominant features of the Earth's geopotential. Spacecraft orbits are affected by the geopotential field; the dominant effects are long-term secular variations in the argument of perigee and right ascension of the ascending node due to the oblateness of the Earth.

To incorporate gravitational forces properly, the Earth's oblate gravitational field can be modeled as a function of Zonal and Tesseral components. The Zonal terms represent an expansion of the geopotential that is latitude dependent. The Tesseral terms represent the geopotential that is both latitude- and longitude-dependent. For this simulation, FreeFlyer was configured to use the "EGM96.potential"[15] data file for modeling the geopotential of Earth with a 20x20 field and point masses for the Moon and Sun.

To predict atmospheric forces on the spacecraft, FreeFlyer used the Jacchia-Roberts 1972 atmospheric density model[16-18] for monthly mean smoothed solar radiation values along with weighted planetary geomagnetic index (Ap) to produce atmospheric density values. Since both ideal and decaying conditions (corresponding to various points during the mission) were tested in CoTherm's simulations, the Schatten files[19] were chosen in place of the Celestrak Space Weather file due to the availability of longer-term predictions. These density model and solar flux predictor file choices (Jacchia Roberts and Schatten, respectively) were used to model both atmospheric drag and lift.

Solar radiation pressure (SRP) was included in the spacecraft's force model using an N-Plate SRP model (diagrammed in Figure 7). The flat plate model approximates the shape of a satellite by a collection of flat plates, each having different reflectivity properties representing various sides of the satellite. In this approach the magnitude of the SRP acceleration will vary depending on the satellite's orientation with respect to the Sun.[20]

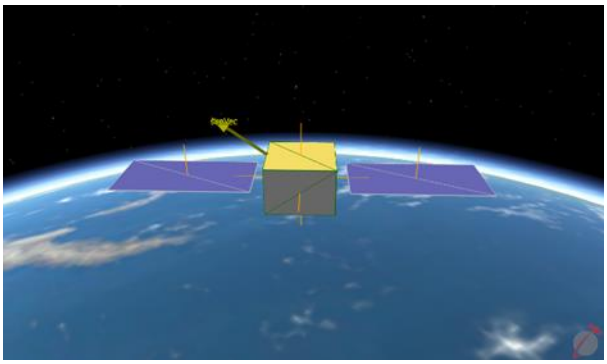

Figure 7: FreeFlyer Plate Model Visualization

The spacecraft's attitude was defined with the z-axis pointing to Earth (Nadir pointing), the x-axis pointing along the spacecraft's velocity vector, and the y-axis as the cross product of the first two axes (diagrammed in Figure 8).

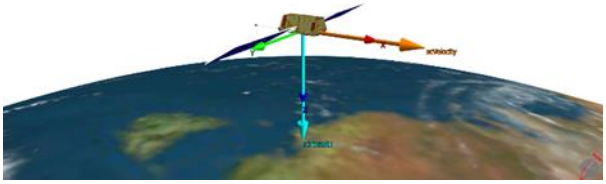

Figure 8: FreeFlyer Spacecraft Attitude Visualization

In FreeFlyer, the spacecraft was propagated first using a Runge Kutta 8(9) integrator with a fixed step size of 60 seconds until it dropped below a 300 km altitude, then, a Bulirsch Stoer integrator was used to finish propagation into Earth's atmosphere. The transition from the Runge Kutta 8(9) integrator to the Bulirsch Stoer integrator was employed for increased fidelity during orbital decay analysis. While propagating the spacecraft, shadow conditions were evaluated and visualized in FreeFlyer. These are diagrammed in Figure 9, with both Body-Fixed and International Celestial Reference Frame (ICRF) views shown to better understand the eclipse conditions (shown in orange).

Figure 9: FreeFlyer Shadow Visualization (Left: Body-Fixed View, Right: ICRF View)

With the configured setup, the spacecraft propagated for nearly eight years before reentering the Earth's atmosphere. The rapid decay in satellite altitude (shown in Figure 10) can be related to the drag force that such a LEO satellite experiences due to its interaction with the relatively few air molecules present.[21] These values are dependent on the current space weather conditions, so, we utilize the Schatten files for futuristic lifetime analysis.

The projected orbit altitude, shown in Figure 10 as a function of elapsed orbit time, starts with an initial value of 546 km (nominally, since the orbit is slightly elliptical). The apparent width of the line is due to the temporal resolution of the propagated orbit; an elliptical orbit whose altitude is sampled every few minutes yields an oscillating value that decays with time, and this elliptical oscillation creates a thick line plot. However, we can see the average orbit altitude decay almost linearly for the first few years, dropping out of LEO by the eighth year. For this work, we selected 7.4 years as

the termination point of our analysis, yielding a final satellite altitude of 400 km.

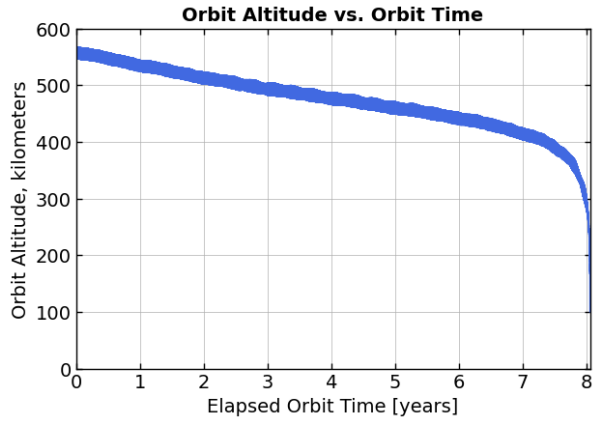

Figure 10: Orbit Altitude vs. Elapsed Orbit Time

For input into the CoTherm process, a custom output text file containing the spacecraft's epoch, position in the Earth Center Earth Fixed (ECEF) reference frame, attitude represented in quaternions, shadow conditions, and the Sun's position with respect to Earth was generated. These values were reported from FreeFlyer to a CSV-formatted text file using 60 second intervals throughout the spacecraft's propagation.

The CoTherm process also has the ability to visualize the spacecraft in orbit, to enhance user understanding of the scenario and ensure orbital inputs are being interpreted correctly between tools. Figure 11 depicts a screen capture from one temporal point in the 3D animation that is generated by CoTherm for the user.

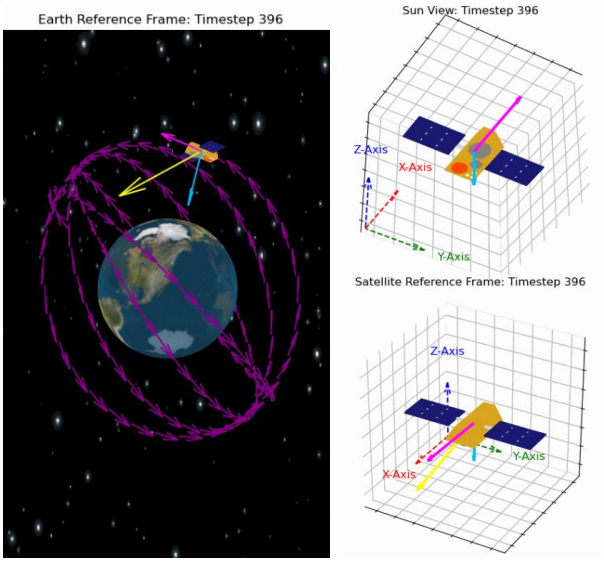

Figure 11: CoTherm-based Orbit Visualization

Battery Lifetime

During the course of the satellite mission the performance of the battery changes as it ages and is also impacted by usage. These two phenomena are referred to as calendar fade and cycling fade, respectively. Additionally, both of these causal factors impact two battery performance characteristics, namely battery internal resistance and battery capacity. First, we address the impact of calendar fade and cycling fade on internal battery resistance.

As the internal resistance of a battery cell increases, the current it is able to accept/supply for charge/discharge purposes (respectively) is reduced, assuming other parameters stay constant. This makes increased internal resistance both undesirable and unavoidable, due to the combined effects of the inevitable aging process (which leads to calendar fade) and necessary mission-based usage (which creates cycling fade).

In addition to increased internal resistance, calendar fade and cycling fade also both contribute to a decrease in battery capacity. Both of these factors influence the relative capacity (compared to the initial, ideal capacity). The total relative capacity is based on the most significant of the two factors for a given scenario; thus, the minimum of the two relative capacities ($Q_{calendar}$ and Q_{cycle}) is taken as the overall relative capacity.

Using a battery lifetime workflow[13] developed and validated by ThermoAnalytics, we use predictions of a battery's thermal history and usage patterns taken from initial dynamic satellite simulations (from the beginning of the mission) to estimate changes to internal battery resistance and capacity as a function of time and cycling. A graphical representation of this process is shown in Figure 12.

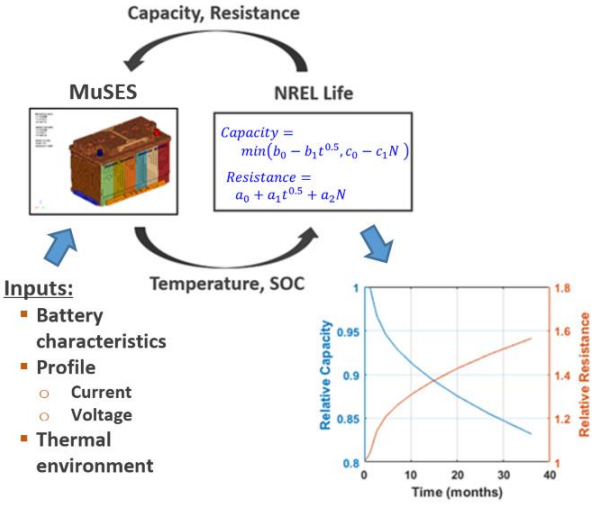

Figure 12: Battery Lifetime Estimation Process

Photovoltaic Radiation Degradation

During a years-long orbit in space, PV modules are exposed to a significant amount of cumulative radiation *in situ*, reducing the efficiency with which they are able to convert solar energy to electrical power. Bombardment by subatomic particles, both protons and electrons, impacts temperature-dependent efficiency as a function of exposure time. By computing an orbit-average McIlwain L-value (which describes a particular set of magnetic field lines) and magnetic field strength, proton and electron flux values can be computed for specified energies. These flux values can then be integrated over mission duration to determine the proton and electron fluence experienced by the satellite over some portion of its lifetime. Typically, PV datasheets[22] include performance data for new modules which may include fluence-based degradation characteristics. Using computed particle flux values and time-integrated fluence values, changes in the nominal efficiency and temperature correction coefficient can be estimated and used to simulate the performance of aged PV modules.

ANALYSIS AND RESULTS

In this section we detail the thermal-electrical results of the various dynamic orbital simulations performed, including a few consecutive orbits at the beginning of the satellite's mission lifetime and several years in the future once the battery and PV modules are partially degraded.

Baseline Thermal-Electrical Results

The initial orbit propagated by FreeFlyer was provided to the CoTherm automation process, and a transient thermal-electrical simulation was performed. To aid visualization of critical environmental boundary conditions that effect temperature results, a representative example of absorbed incident solar flux (in units of W/m^2) is shown in Figure 13 for a single timestep during the initial baseline transient simulation.

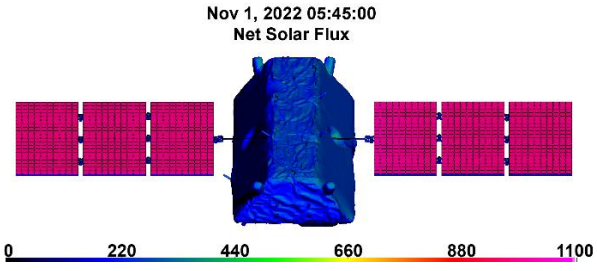

Figure 13: Example of Absorbed Incident Solar Flux (W/m^2) Prior to PV Energy Conversion

Temperature results for a different timestep (15 minutes later, and from a different perspective) are shown in Figure 14 with a high contrast false-color palette applied.

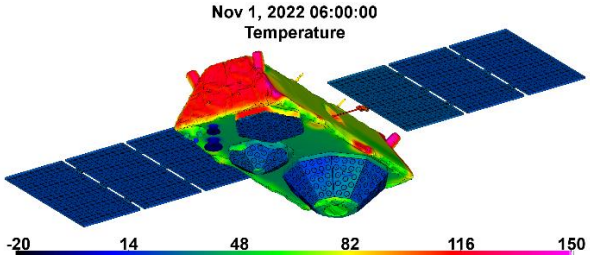

Figure 14: Example of Exterior Temperatures (°C) for the Baseline Simulation

Some of the most interesting results from the baseline simulation are plotted automatically by the CoTherm process, to aid understanding of the satellite's electrical performance. An example of these results is depicted in Figure 15. In the upper-left, Panel (a) displays the average temperature of the PV modules throughout several orbital cycles. The temperature oscillation is governed by the absorbed solar energy, thermal energy radiated from Earth, radiation loss to space and the thermal capacitance of the panels. These PV panel temperatures impact the photovoltaic module efficiency, shown in Panel (b), as does the solar incidence angle.

Below these two green plots, the average battery cell temperature and battery pack current are indicated in Panel (c) and Panel (d), respectively. Positive battery current values show regions of battery charging, and negative battery current values represent regions of battery discharge. Orbit segments where battery current is exactly zero indicate a battery that is either fully charged (and thus needs no charging) or fully discharged (and is unable to provide a current). Note that while additional thermal control strategies could have been incorporated to manage battery pack temperature shown in Panel (c) differently, the baseline configuration was left in place to better demonstrate the impacts of battery cell degradation.

In the lower left Panel (e), the SoC (state of charge) of the battery pack is displayed. An initial (pessimistic) charge level of 50% was assumed, and the SoC is observed to increase during sunlit orbit segments and decrease when the battery must be discharged during eclipsed regions. At several points in the orbital period shown, the SoC reaches a maximum value (near a specified 90%) where the battery pack is fully charged.

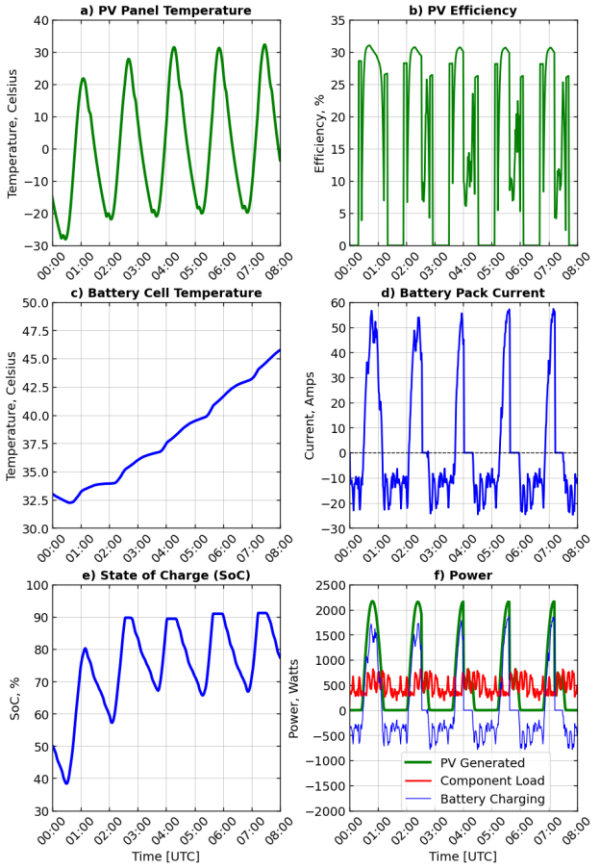

Figure 15: Baseline Battery & PV Results

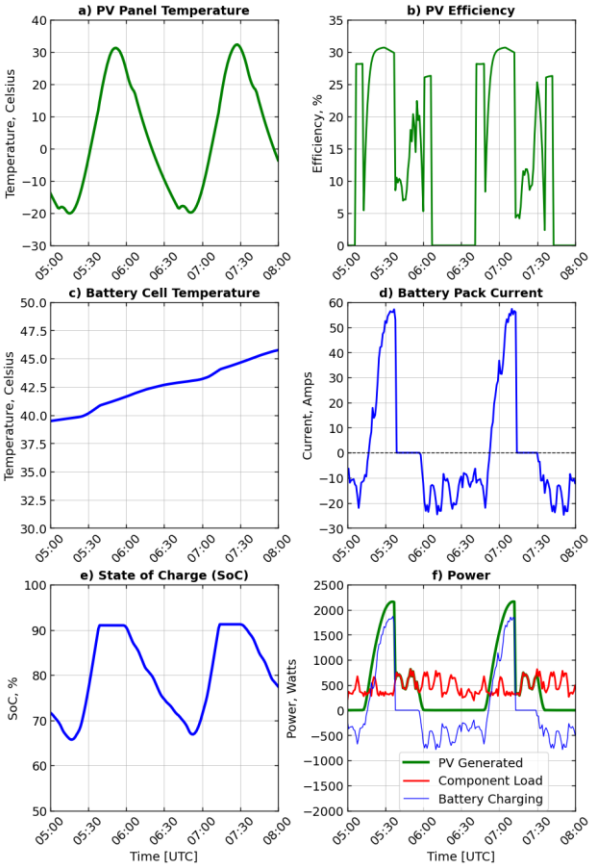

Figure 16: Baseline Results (Final 3 Hours)

Panel (f) shows multiple power curves. These include the photogenerated power converted by the PV module (shown in green), the total power load required by the active components (plotted in red), and the battery charge/discharge power (graphed in blue). This battery power is shown as positive when the pack is charged by the excess solar energy (beyond what the active components require), negative when the battery must be discharged due to a lack of sunlight, and zero when the battery pack is fully charged.

To improve the legibility and clarity of the baseline thermal-electrical results, only the final three orbital hours of the transient simulation are shown in Figure 16. This allows for the display of approximately two orbit periods, hides the initial simulation segment where the impact of initial conditions fades, and shifts the focus to the expected orbital cycle of interest.

Examining Figure 16, we see a PV module temperature in Panel (a) that oscillates between -20°C and 32°C, which is dependent on a number of factors including the thermal capacitance of the panel. Panel (b) shows the PV panel efficiency vary about the nominal value of 29% due to module temperature and solar incidence angle. The pack current alternates between charging and discharging in Panel (d), reaching peak charging values of 57 Amps and discharge values of -24 Amps. The SoC of the battery pack, shown in Panel (e), varies in a stable range from 67% during eclipses to "full" charge during sunlit orbital segments. Finally, Panel (f) indicates the efficiency-based solar power harvested by the PV modules, component load required by the satellite mission and the battery charge/discharge power. Note that the PV-harvested power peaks around 2160 Watts, and the battery charging power peaks at 1800 Watts while the discharge power reaches 750 Watts (negative sign indicating discharge status). These results were obtained for the baseline case of satellite thermal-electrical performance at the beginning of its mission life; from here we next proceed to analyze the impact that the remainder of the mission has on battery and PV operations, and ultimately on how the satellite system performs.

Analysis of Battery Lifetime

As previously stated in the Methodology section and depicted in Figure 12, cycling and calendar fade impact battery performance by increasing internal resistance and reducing capacity. Estimation of reduced battery capacity and increased internal resistance was performed using the initial satellite simulation results as inputs (i.e., battery pack temperature and current results; see Figure 16). Due to the elevated thermal conditions and relatively minimal cycling experienced during this LEO mission, calendar fade contributes more significantly than cycling fade to battery pack degradation.

The internal resistance scaling factor calculated for the LEO used for this work, shown with a dashed orange line on the right-hand *y*-axis of Figure 17, starts at an initial value of 1 (since it is normalized relative to its initial resistance) and increases over time. Three years into the mission, the internal resistance scaling factor has increased to a value of 1.21. This mid-mission point will be used to present semi-degraded results in a subsequent section, demonstrating spacecraft performance below that observed immediately after initial launch but less degraded than just prior to atmospheric reentry. By the time the satellite has been in orbit for 7.4 years − the terminal point selected based on Figure 10 − the internal resistance scaling factor has increased to 1.34.

The expected reduction in relative pack capacity, the other battery degradation factor of import, can also be predicted by the aforementioned battery lifetime workflow. At a point three years into the mission, the relative battery capacity will have decreased to 0.870 as observed on the left-hand y-axis of Figure 17. This results in a capacity of 47 A-hr, which is 87% of the initial 54 A-hr. At the selected termination point of this LEO study (chosen to be 7.4 years based on Figure 10) the relative battery capacity will have decreased to 0.774. For a battery pack that begins its mission at 54 A-hr, a relative capacity of 77.4% near the end of the mission equates to 41.8 A-hr, effectively.

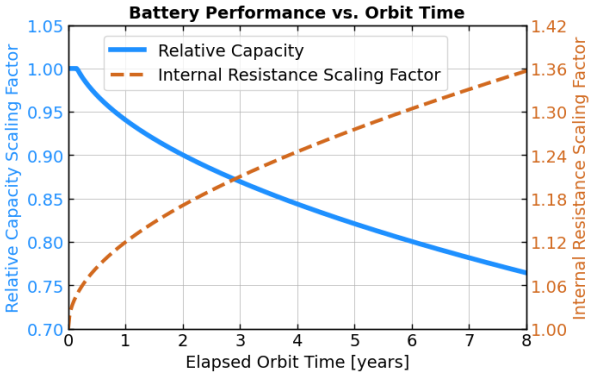

Figure 17: Battery Performance vs. Orbit Time

Based on this battery lifetime analysis, the end-of-mission simulation results (performed to predict the thermal-electrical satellite results 7.4 years after launch) assume an internal resistance scaling factor of 1.34 and a pack capacity of 41.8 A-hr. For the purposes of obtaining a temporal data point somewhere between 0 and 7.4 years, another satellite simulation was performed at the three-year point. These mid-mission results assume an internal resistance scaling factor of 1.21 and a battery capacity of 47 A-hr.

Analysis of PV Radiation Degradation

As was mentioned before, subatomic particle bombardment induces radiation degradation in space-deployed PV modules. The proton and electron radiation impact on PV performance depends on a number of variables that must be calculated or estimated for a given orbit. Fluence (for electrons or protons) is a function of electron flux (integrated over time), and flux can be computed as a function of *L*-value, B/B_0 and energy values. The B/B_0 term signifies the magnetic field intensity normalized by the intensity at the magnetic equator, and *L*-shell values describe a set of planetary magnetic field lines. Both B/B_0 values and *L*-values vary with latitude due to the structure of the Earth's magnetic field.

A range of B/B_0 values that cover all relevant latitudes in the orbit of interest can be generated using an online International Geomagnetic Reference Field (IGRF) calculator.[23] Similarly, the same IGRF calculator can be used to generated a range of altitude-based *L*-values. For this analysis, the orbit supplied by FreeFlyer was used to estimate B/B_0 and *L*-shell value, and these values were averaged to determine representative values to use for flux calculations. Average values of $L = 1.6$ and $B/B_0 = 3$ were computed as a result of this latitude-averaging process; these values were used with an online radiation belt flux calculator[24] to evaluate radiation belt effects and calculate the mean photon flux experienced by the satellite as a function of proton energy (see Table 2).

Table 2: Estimated Proton Flux and Fluence

L	B/B_0	Energy (MeV)	Proton Flux (p/cm²/sec)	Elapsed Orbit Time (years)	Proton Fluence (p/cm²)
1.6	3	0.1	503	3	4.76 E10
1.6	3	1	493	3	4.67 E10
1.6	3	10	398	3	3.77 E10
1.6	3	0.1	503	7.4	1.17 E11
1.6	3	1	493	7.4	1.15 E11
1.6	3	10	398	7.4	9.30 E10

These flux values were then integrated over elapsed orbit time to compute proton fluence values for the various proton energy levels experienced simultaneously by the LEO satellite. This was done for two temporal points in the mission lifetime, once at a time 3 years into the mission, and again 7.4 years after satellite launch.

These proton fluence levels, shown in the rightmost column of Table 2, can then be used with a relevant PV module datasheet[22] to determine[25] the proton-induced impacts on PV efficiency. Using the energy levels and proton fluence values for both 3 and 7.4 years into the orbit, PV efficiency scaling factors were linearly-interpolated from datasheet values to obtain the rightmost two columns (P_M and relative efficiency) of Table 3. P_M displays the maximum power after exposure to the listed proton fluence relative to the maximum power at beginning of life. Relative efficiency displays the efficiency due to the combined effect of protons of different energy levels relative to beginning of life. Note that the relative efficiency column assumes that nominal PV efficiency is scaled by the product of the three P_M values (one for each energy level). Thus, at 3 years into the mission, a relative efficiency of 0.811 was obtained; assuming a nominal PV efficiency of 29%, this yields a revised nominal PV efficiency of 23.5%. At 7.4 years into the mission, a degraded (nominal) PV efficiency of 18.2% was computed. This fluence-based method is not the only technique[25] available for PV degradation calculations, but was used for this work because of the performance parameters set forth in the PV datasheet[22] of interest.

Table 3: Proton-Induced Efficiency Impact

L, B/B_0	Energy (MeV)	Elapsed Orbit Time (years)	Proton Fluence (p/cm^2)	P_M	Relative Efficiency
1.6, 3	0.1	3.0	4.76 E10	0.86	0.811
1.6, 3	1	3.0	4.67 E10	0.94	
1.6, 3	10	3.0	3.77 E10	1.0	
1.6, 3	0.1	7.4	1.17 E11	0.72	0.628
1.6, 3	1	7.4	1.15 E11	0.89	
1.6, 3	10	7.4	9.30 E10	0.98	

The above information in Table 3 is for proton bombardment only; electron impacts must also be considered. However, assuming the same values of L and B/B_0, electron fluence was calculated to be several orders of magnitude smaller than what would be significant for the orbit of interest. For example, at 3 and 7.4 years into the mission, electron fluence values of 4.04E11 and 9.96E11 e/cm^2 were calculated (respectively) for an assumed energy level of 1 MeV. These electron fluence levels are small enough to make only marginal differences in PV efficiency and temperature coefficients, so electron fluence effects were ignored for the degraded simulations performed for this work. Note that any potential impact of proton radiation on temperature coefficients was not reported in the datasheet.

Semi-Degraded Thermal-Electrical Results

Determining the thermal-electrical performance of the satellite system 3 years into the mission required several simulations changes to be made. First, the orbit altitude was reduced to 491 km to match the expected altitude decline seen in Figure 10. Next, the PV efficiency was reduced from the nominal datasheet value of 29% to 23.5% based on the values found in Table 3. The temperature correction parameter found in the PV configuration was left unmodified since electron fluence was deemed insignificant for this analysis. Finally, the battery capacity was reduced to 47 A-hr (87% of the original 54 A-hr capacity) and the internal resistance scaling factor was increased to 1.21 based on Figure 17. The results of this "semi-degraded" orbital simulation, which represents a time 3 years after the initial satellite launch, are shown in Figure 18.

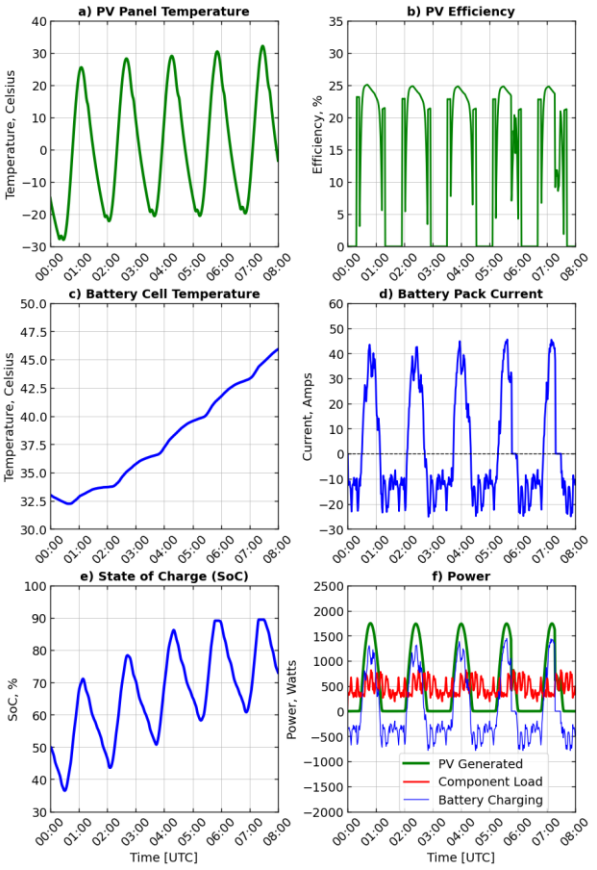

Figure 18: Semi-Degraded Battery & PV Results

To better visualize the impacts of PV and battery degradation, the *x*-axis of Figure 19 (a zoomed version of Figure 18) was limited to the final three hours of the transient simulation. While the PV panel temperature remained relatively unchanged, the PV efficiency shown in Panel (b) is observed to be lower than the baseline (beginning of mission) plots shown previously (see Figure 16). Battery cell temperature is slightly changed from the baseline case, but a reduction in battery pack charging current depicted in Panel (d) is of more interest. Charging current peaks around 45 Amps, a decrease from the peak values of 57 Amps seen in Figure 16. This charge current reduction is a result of less surplus power being generated by the PV module, which is caused by the lower PV efficiency in Panel (b). The SoC variations portrayed in Panel (e) are telling, as the time it takes to reach full charge is longer than in the baseline scenario. Additionally, a larger amplitude (wider swing in min/max values) can also be observed; this is caused by a reduced battery capacity relative to the baseline case. Finally, Panel (f) shows both a reduction in PV-converted power and consequently a reduction in surplus energy used to charge the battery during sunlit times.

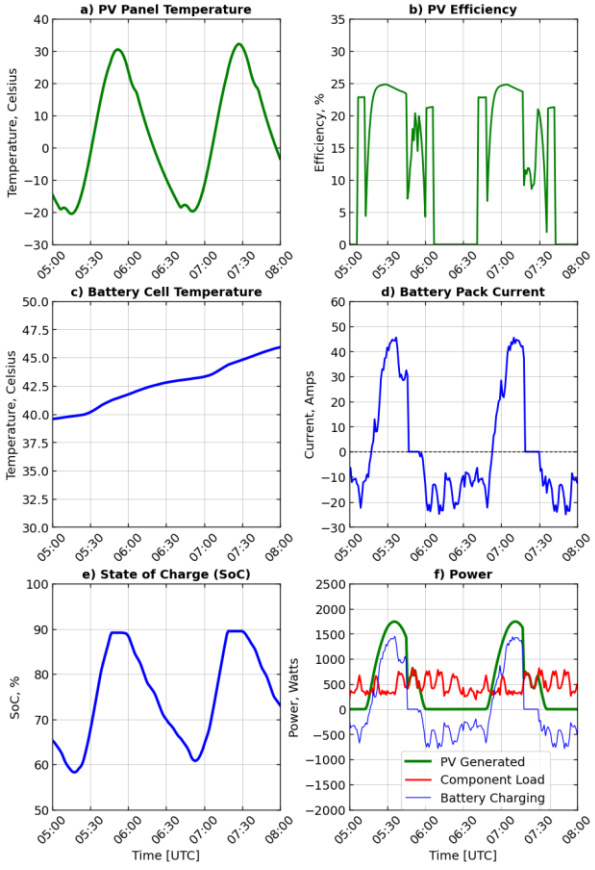

Figure 19: Semi-Degraded Results (Final 3 Hours)

Next, we present the thermal-electrical results closer to the end of the satellite mission lifetime to see the impacts of further battery and PV degradation.

Degraded Thermal-Electrical Results

To present a third temporal snapshot of satellite performance, we selected a time 7.4 years after the initial launch. Based on Figure 10 an orbit altitude of 400 km was used for the thermal simulation, which impacts view factors and radiation exchange between the Earth and the satellite. The battery capacity was reduced from 54 A-hr to 41.8 A-hr, 77.4% of the original capacity based on the findings shown in Figure 17. The internal resistance scaling factor used for the battery pack was increased to 1.34 (from an initial value of 1.0).

For the PV module, the original (nominal) PV efficiency of 29% was reduced to 18.2% based on the proton fluence-based efficiency scaling factors presented in Table 3. Once these altitude, PV and battery changes were incorporated, the multi-orbit dynamic simulation was re-run. The results of this final "degraded" scenario are shown in Figure 20.

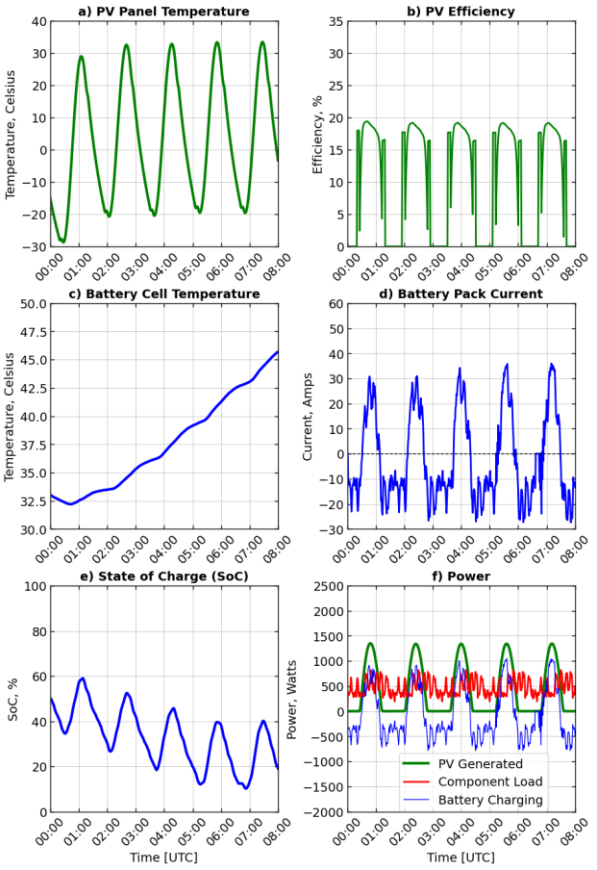

Figure 20: Degraded Battery & PV Results

For increased clarity of PV and battery degradation results, the *x*-axis of Figure 21 (a zoomed version of Figure 20) was limited to the final three hours of the transient simulation. Again, the PV panel temperature remained relatively unchanged, but the PV efficiency shown in Panel (b) is observed to be even lower than the baseline plots shown previously (see Figure 16) to represent expectations for performance at the beginning of the mission.

Battery cell temperature is only slightly changed from the baseline case; a further reduction in battery pack charging current depicted in Panel (d) is of more interest. Charging current peaks around 35 Amps, a major decrease from the peak values of 57 Amps seen in Figure 16. This charge current reduction is primarily a result of much less surplus power being generated by the PV module compared to the beginning of the mission, which is caused by the significantly lower PV efficiency illustrated in Panel (b).

The SoC decline portrayed in Panel (e) compared to that displayed in Figure 16 and Figure 19 shows that, due to insufficient charging during sunlit portions and reduced capacity to power electronics during eclipsed times, the overall SoC trend indicates that the PV/battery degradation has rendered the overall system close to being insufficient to maintain mission objectives. The minimum SoC is approximately 10%, very near the SoC limiter cutoff which would mean end-of-life for the battery pack has been reached. Indeed, it is possible that by simulating more than five orbits (thus extending the transient analysis further) the SoC might have reached the minimum cutoff value had a relatively generous initial SoC of 50% not been chosen for comparative purposes.

Finally, Panel (f) shows both a reduction in PV-converted power (green curve) and consequently a reduction in surplus energy used to charge the battery (blue line) during sunlit times.

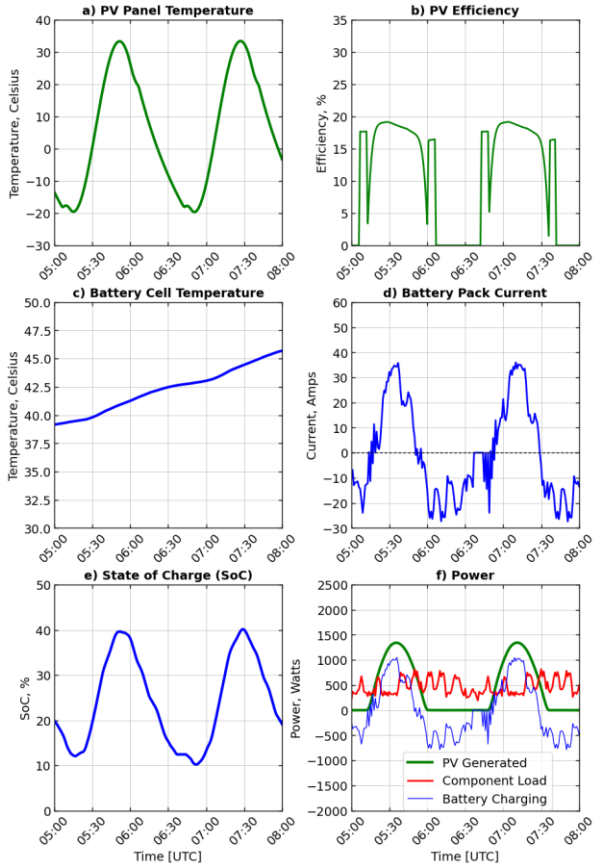

Figure 21: Degraded Results (Final 3 Hours)

Thermal-Electrical Results over Mission Lifetime

Since these results are spread over multiple figures that span several pages, the most relevant figures of merit are compiled together and displayed in Figure 22. Panel (a) shows a steady decline in PV efficiency from the initial, nominal value to values that have been reduced to approximately 81% and 63% of the initial efficiency. Similarly, the reduction in PV-generated power is evident in Panel (b), as well as how many orbits it takes for the battery to fully charge (assuming an initial SoC of 50% in all cases) and thus modify the PV power generation shape from the expected symmetric curve when the maximum PV-harvested power is not required. The upper-most green curve (representing t = 0 years) shows the PV controller reducing power generation by the second sunlit orbit segment. The blue curve (representing t = 3 years) shows this happen during the fourth sunlit segment, and the red line (t = 7.4 years) never hits this point during the 8 hour (~5 obit) simulation.

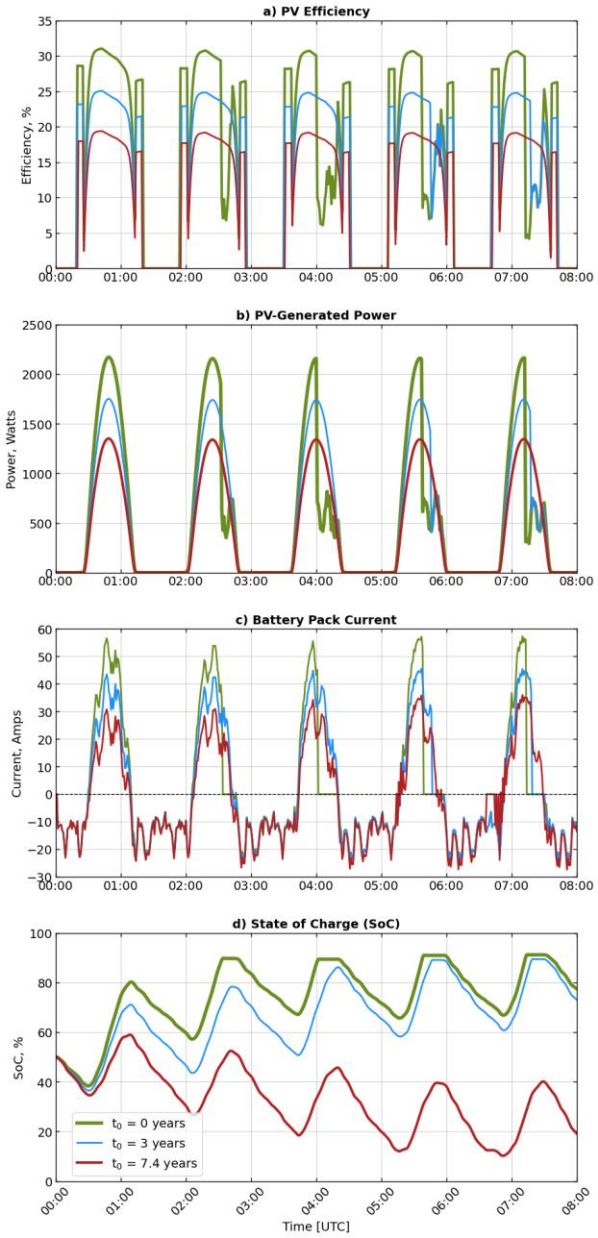

Figure 22: Results from Multiple Mission Lifestages

This also occurs in Panel (c) where the peak battery pack charging current is reduced over the mission lifetime. The zero-valued current regions illustrate when charging is not occurring due to full-charge SoC status as determined by the SoC limiter. Finally, Panel (d) shows the SoC as a function of both simulation time (during a multi-orbit scenario) and elapsed mission time (t = 0, 3 and 7.4 years). The start-of-mission SoC line shows an upward trend where the battery is fully charged around 2.5 hours into the simulation, and the SoC oscillates between 90% and 65% at the end (equilibrium state) of the simulation. The mid-mission (blue) line show a SoC of 90% not being exceeded until close to six hours into the simulation, and a 60-90% SoC range being required (due to the reduced battery capacity). The final mission point shown in Panel (d) indicated a downward SoC trend from the initial value of 50% towards a steady-state oscillation between 10% and 40% charged.

SUMMARY

To ensure that a satellite can fulfill its intended mission, several essential design choices must be considered carefully. PV modules with sufficient surface area and energy conversion efficiency are required for supplying power to the spacecraft. Additionally, a battery pack with enough capacity to power active components during eclipsed orbit segments must be selected. However, the performance of battery cells and PV modules deteriorates over time, necessitating a predictive approach for determining that vital subsystems like battery packs and PV modules can fulfill their duties over their intended service life in orbit.

In this work we demonstrate a workflow for predicting the thermal-electrical capabilities of a satellite over the course of its lifetime. This process uses an orbit propagation tool (which considers gravitational and atmospheric forces as well as solar radiation pressure) to determine the precise dynamic position and attitude of the spacecraft, Earth and sun. This orbit is supplied to a high fidelity multi-physics solver which incorporates PV energy conversion, battery charging and discharging while computing transient temperatures for all internal and external components. The system state-of-health over the course of a multi-year mission is estimated by projecting PV degradation and battery deterioration into the future.

We illustrate the criticality of assessing spacecraft battery lifetime and PV efficiency decline by quantifying the charge status at three distinct mission points (see Figure 22 for a graphical summary of this). The reduction in PV-converted power yields less charging current and, consequently, lower state-of-charge (SoC). As battery capacity decays and internal resistance increases, the spacecraft becomes less able to power its active components sustainably. This becomes evident as the SoC trend switches from the initial upward climb to an unmaintainable downward trend.

However, thermal management strategies and orbit control factors can help prolong the service life of a satellite, and the approach presented here can be used to evaluate the efficacy of such tactics. For example, station keeping and orbital adjustments can modify solar incidence angles, which can impact battery charging/discharging, PV efficiency and temperature gradients across the spacecraft. The thermal environment of a battery impacts the rate at which it ages, so

passive/active thermal control techniques and orbital attitude adjustments can help extend the lifetime of a battery pack. This means that subsystem design choices and in-orbit adjustments can positively influence the serviceable duration of a satellite, and the predictive methodology described here is capable of forecasting the benefits of various strategies.

Acknowledgments

The authors wish to acknowledge the contributions of Luke Marttila and Eli Datema to the geometry used for this effort, and to Tim Viola, Derrick Levanen and Eric Marttila for advice regarding initial simulations performed during the early stages of this work.

References

1. Johnson, K., Curran, A., Less, D., Levanen, D., Marttila, E., Gonda, T. and Jones, J., "MuSES: A New Heat and Signature Management Design Tool for Virtual Prototyping," Ninth Annual Ground Target Modeling & Validation Conference, Houghton, MI, August 1998.
2. Sanders, J., Johnson, K., Curran, A., and Rynes, P., "Ground target infrared signature modeling with the multiservice electro-optic signature (MuSES) code," Proc. SPIE Targets and Backgrounds VI: Characterization, Visualization, and the Detection Process 4029, 197 (2000).
3. Packard, C., Viola, T., Klein, M., "Hyperspectral target detection analysis of a cluttered scene from a virtual airborne sensor platform using MuSES", Proc. SPIE Vol. 10432, Target and Background Signatures III, 1043208 (October 17, 2017), doi:10.1117/12.2278172.
4. Packard, C., Golubev, T., Woodford, D., Rosiek, M., "Small Satellite Validation of a Simulation Approach for Assessing Dynamic Temperatures in Orbit", 52nd International Conference on Environmental Systems, 16-20 July 2023, Calgary, Canada.
5. Peck, S. and Pierce, M., "Development of a temperature-dependent Li-ion battery thermal model", SAE Technical Paper 2012-01-0117, 2012, https://doi.org/10.4271/2012-01-0117.
6. Peck, S., Olszanski, T., Zanardelli, S. and Pierce, M., "Validation of a Thermal-Electric Li-Ion Battery Model," *SAE Int. J. Passeng. Cars - Electron. Electr. Syst.*, Vol. 5(1), 2012, doi:10.4271/2012-01-0332.
7. Peck, S., Velivelli, A., and Jansen, W., "Options for Coupled Thermal-Electric Modeling of Battery Cells and Packs," *SAE Int. J. Passeng. Cars – Electron. Electr. Syst.*, Vol. 7(1), 2014, doi:10.4271/2014-01-1834.
8. Golubev, T. and Lunt, R.R., "Evaluating the Electricity Production of Electric Vehicle-Integrated Photovoltaics via a Coupled Modeling Approach", 2021 IEEE 48th Photovoltaic Specialists Conference (PVSC), 20-25 June 2021.
9. Yao, L., Xu, S., Tang, A., Zhou, F., Hou, J., Xiao, Y., Fu, Z., et al., "A Review of Lithium-Ion Battery State of Health Estimation and Prediction Methods", *World Electric Vehicle Journal*, 2021, Volume 12 (3), 113.
10. Li, Y., Liu, K., Foley, A., Zulke, A., Berecibar, M., Nanini-Maury, E., Van Mierlo, J., Hoster, H., "Data-driven health estimation and lifetime prediction of lithium-ion batteries: A review", *Renewable and Sustainable Energy Reviews*, Vol. 113 (2019).
11. Smith, K., Saxon, A., Keyser, M., Lundstrom, B., Cao, Z., Roc, A., "Life Prediction Model for Grid-Connected Li-ion Battery Energy Storage System", 2017 American Control Conference, 24-26 May 2017, Seattle, WA.
12. Maurilio, J., Bazmohammadi, N., Vasquez, J., Guerrero, J., "A short review of radiation-induced degradation of III–V photovoltaic cells for space applications," Solar Energy Materials and Solar Cells, Vol. 233, 2021.
13. Lim, Y., Edel, Z., Marker, E., Joung, S. et al., "Data-Driven Battery Lifetime Model Calibration and Analysis for an Electric Vehicle Battery's Durability Performance," SAE Technical Paper 2024-01-2281, 2024, doi:10.4271/2024-01-2281.
14. Demars, C., Packard, C., Tyler, D., Rodgers, C., "High-Fidelity Simulation of Dynamic Thermal Satellite Signatures with MuSES", Proc. of the Advanced Maui Optical and Space Surveillance Technologies (AMOS) Conference, Sept 2023.
15. Lemoine, F.G., Kenyon, S.C., et al., NASA Goddard Space Flight Center, Greenbelt, Maryland, 20771 USA (1998).
16. Jacchia, L.G., "Revised Static Models of the Thermosphere and Exosphere with Empirical Temperature Profiles," Smithsonian Astrophysical Observatory Special Report No. 332 (1971).
17. Roberts, E. R. Jr., "An Analytical Model for Upper Atmosphere Densities Based Upon Jacchia's 1970 Models, Celestial Mechanics," Volume 4, Issue 3-4, 368-377 (1971).

18. "Goddard Trajectory Determination System (GTDS) Mathematical Theory", FDD/552-89/001 and CSC/TR-89/6001, July 1989.

19. Schatten. K., “Solar Activity for use in Orbit Prediction”, Flight Mechanics Symposium (2001).

20. Farrés, A., Folta D. and Webster C., "Using Spherical Harmonics to Model Solar Radiation Pressure Accelerations," AAS/AIAA Astrodynamics Specialist Conference (2017).

21. Kennewell, J. “Satellite Orbital Decay Calculations”, IPS Radio & Space Services, 1999.

22. CESI S.p.A. CTJ30-1 Datasheet. (2020) From https://www.cesi.it/app/uploads/2020/03/Datasheet-CTJ30-1.pdf.

23. International Geomagnetic Reference Field (IGRF) calculator. (2024). Retrieved from https://ccmc.gsfc.nasa.gov/modelweb/models/igrf_vitmo.php

24. AE-8/AP-8 Radiation Belt Models online calculator. (2024). Retrieved from https://ccmc.gsfc.nasa.gov/modelweb/models/trap.php.

25. Li J., Aierken A., Liu Y., Zhuang Y., Yang X., Mo J. H., Fan R.K., Chen Q.Y., Zhang S.Y., Huang Y.M. and Zhang Q, "A Brief Review of High Efficiency III-V Solar Cells for Space Application", *Frontiers in Physics* Vol. 8, 2021, doi: 10.3389/fphy.2020.631925.